Hydrocarbon chemistry in the inner regions of planet-forming disks

Kanwar, J.; Kamp, I.; Woitke, P.; Rab, Ch; Thi, W. F.; Min, M.

Published in:
Astronomy & Astrophysics

DOI:
10.1051/0004-6361/202346262

Publication date:
2024

A&A, 681, A22 (2024)
https://doi.org/10.1051/0004-6361/202346262

Astronomy & Astrophysics

Hydrocarbon chemistry in the inner regions of planet-forming disks

J. Kanwar[1,2,3], I. Kamp[1], P. Woitke[2], Ch. Rab[4,5], W. F. Thi[4], and M. Min[6]

[1] Kapteyn Astronomical Institute, University of Groningen, PO Box 800, 9700 AV Groningen, The Netherlands
e-mail: kanwar@astro.rug.nl
[2] Space Research Institute, Austrian Academy of Sciences, Schmiedlstr. 6, 8042, Graz, Austria
[3] TU Graz, Fakultät für Mathematik, Physik und Geodäsie, Petersgasse 16, 8010 Graz, Austria
[4] Max Planck Institute for Extraterrestrial Physics, Giessenbachstrasse, 85741 Garching, Germany
[5] University Observatory, Faculty of Physics, Ludwig-Maximilians-Universität München, Scheinerstr. 1, 81679 Munich, Germany
[6] SRON Netherlands Institute for Space Research, Niels Bohrweg 4, 2333 CA Leiden, The Netherlands

Received 27 February 2023 / Accepted 30 September 2023

ABSTRACT

Context. The analysis of the mid-infrared spectra helps understanding the composition of the gas in the inner, dense and warm terrestrial planet forming region of disks around young stars. ALMA has detected hydrocarbons in the outer regions of the planet forming disk and *Spitzer* detected C_2H_2 in the inner regions. JWST-MIRI provides high spectral resolution observations of C_2H_2 and a suite of more complex hydrocarbons are now reported. Interpreting the fluxes observed in the spectra is challenging and radiation thermo-chemical codes are needed to properly take into account the disk structure, radiative transfer, chemistry and thermal balance. Various disk physical parameters like the gas-to-dust ratio, dust evolution including radial drift, dust growth and settling can affect the fluxes observed in the mid-IR. Still, thermo-chemical disk models were not always successful in matching all observed molecular emission bands simultaneously.

Aims. The goal of this project is two-fold. Firstly, we analyse the warm carbon chemistry in the inner regions of the disk, namely within 10 au, to find pathways forming C_2H_2 potentially missing from the existing chemical networks. Secondly, we analyse the effect of the new chemistry on the line fluxes of acetylene.

Methods. We used the radiative thermo-chemical disk code called PRODIMO to expand the hydrocarbon chemistry that occurs in a typical standard T Tauri disks. We used the UMIST and the KIDA rate databases for collecting reactions for the species. We included a number of three-body and thermal decomposition reactions from the STAND2020 network. We also included isotopomers for the species that were present in the databases. The chemistry was then analysed in the regions that produce observable features in the mid-infrared spectra. We studied the effect of expanding the hydrocarbon chemistry on the mid-infrared spectra.

Results. Acetylene is formed via two pathways in the surface layers of disks: neutral-neutral and ion-neutral. They proceed via the hydrogenation of C or C^+, respectively. Thus, the abundances of C, C^+, H and H_2 affect the formation of C_2H_2. Therefore, also the formation of H_2 indirectly affects the abundance of acetylene. Chemisorbed H is more efficient in forming H_2 compared to physisorbed H at warm temperatures and hence increases the abundance of C_2H_2.

Conclusions. We provide a new extended warm chemical network that considers up to eight carbon atom long species, while also taking into account different isotopomers and can form the building blocks of PAHs: C_6H_6. For a standard T Tauri disk with a canonical value of gas-to-dust mass, the line fluxes increase only by a factor of less than 2. JWST is now detecting hydrocarbons such as methane, acetylene, and C_4H_2 in disks with a high C/O ratio. Hence, this new extended warm hydrocarbon network will aid in interpreting the observed mid-infrared fluxes.

Key words. astrochemistry – protoplanetary disks – methods: numerical

1. Introduction

The inner region of a planet-forming disk (∼10 au) is warm (200–1000 K) and dense (10^8–10^{15} cm^{-3}), and it serves as the nursery for terrestrial planets (Henning & Semenov 2013). Understanding the rich molecular chemistry in this region can help predict the composition of terrestrial planets. Studies of the chemistry in this region have been made possible with mid-infrared spectroscopy, which traces the warm surface layers.

Carbon is one of the most abundant elements and it is essential for life. The warm molecular layer is abundant in H_2, carbon and shielded from UV photons by dust, H_2 (Draine & Bertoldi 1996), H_2O (Bethell & Bergin 2009; Duval et al. 2022), thus paving the way for a rich organic chemistry. Carbon based molecules like CO, CO_2, C_2H_2 have been observed using *Spitzer* (e.g. Carr & Najita 2011; Salyk et al. 2008; Pontoppidan et al. 2010). Other hydrocarbons such as c-C_3H_2 (Qi et al. 2013), C_2H (Bergin et al. 2016) have been detected in the outer disks by the MAPS consortium (Ilee et al. 2021; Guzmán et al. 2021). With the advent of JWST, a plethora of new species have been discovered due to its high sensitivity and increased spectral resolution, as compared to *Spitzer*. Among the new detections (Tabone et al. 2023, Arabhavi & Kamp 2023), there are various hydrocarbons emitting in the mid-infrared region, as predicted by Bast et al. (2013).

There have been various studies on hydrocarbon chemistry in different environments (temperatures, pressures initial abundances, radiation, etc.) as in molecular clouds, AGB stars,

planetary nebulae, and planet forming disks. Carbon chains can form at the early stages of cloud evolution before C gets locked in CO in warm carbon chain chemistry in molecular clouds. An experimental study carried out by Santoro et al. (2020) investigated the gas-phase interaction of C and C_2 with C_2H_2 leading to polyacetylenic chains and poly-cyclic aromatic hydrocarbons (PAHs) for the outer layers of C-rich AGB and protoplanetary nebulae. Benzene is shown to form in a bottom up approach in the inner 3 au of the planet forming disk and its abundance structure is affected by the uncertainty in the adsorption energies assumed for it (Woods & Willacy 2007). Kress et al. (2010) studied the formation of poly-cyclic aromatic hydrocarbons (PAHs) and calculated the position of the soot line beyond which PAHs are destroyed in disks. A comparative study on chemistry around the stars with spectral types from A to M showed different abundance structures for C_2H_2 and sets of pathways leading to its formation in X-ray and UV-dominated regions (Walsh et al. 2015).

Hydrocarbons have been detected in the ISM and molecular clouds, with only C_2H_2 detected in disks around T Tauri stars and CH_4, C_4H_2, C_6H_6 detected (Tabone et al. 2023) in disks around very low-mass stars in the mid-IR. There have been numerous attempts to reproduce the observational flux levels through thermo-chemical modelling. Earlier works (e.g. Woitke et al. 2018; Greenwood et al. 2019a,b; Anderson et al. 2021) have proposed high gas-dust, dust evolution (including radial drift, growth, settling), and a high C/O ratio to interpret the observed fluxes of C_2H_2 and H_2O. Little work has gone into taking a more detailed look into the formation pathways of C_2H_2. This basis explains the need to revisit the chemical networks used widely in the disk community.

In this paper, the focus is to expand on hydrocarbon chemistry and study how it affects the mid-infrared spectra especially in the light of new JWST data. We used the radiation thermo-chemical modelling code PRODIMO (Woitke et al. 2009) to determine the disk structure of a typical T Tauri disk (Woitke et al. 2016). The hydrocarbon chemistry is expanded beyond the large DIANA chemistry (Kamp et al. 2017). The key ingredients of the disk modelling code PRODIMO, the large DIANA chemical network and the description of the extension of the chemical network for hydrocarbons is provided in Sect. 2. Section 3 identifies pathways of C_2H_2 formation, presents network diagrams and analyses the hydrocarbon chemistry in a typical T Tauri disk and highlights the differences between using the UMIST (McElroy et al. 2013) and the KIDA (Wakelam et al. 2012)[1] chemical rate databases. The implications of the new chemical network on the mid infrared spectra is described in Sect. 4. Section 5 discusses the results, followed by conclusions.

2. Modeling

2.1. Physical disk modeling

PRODIMO (Version: 2.0-421754a9) is a radiation thermo-chemical code that models the physical and chemical structure of planet forming disks (Woitke et al. 2009, 2016). It assumes an axis-symmetric, Keplerian, irradiated disk. It performs 3D ray-based dust continuum radiative transfer to obtain the dust temperature and the wavelength dependent radiation field in the disk (Woitke et al. 2009).

[1] We use the published network file kida.uva.2014 from Wakelam et al. (2015), referred to as KIDA2014 in the remainder of this work.

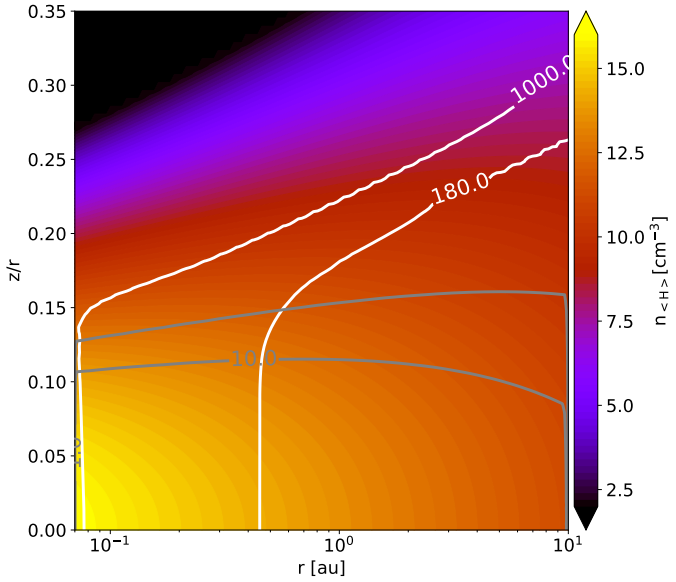

Fig. 1. Particle density ($n_{<H>}$) of the disk in all the subsequent models. The white lines corresponds to the gas temperature of 180 K and 1000 K. The gray contours depict the combined radial and vertical A_V = 1 and A_V = 10.

We model a steady-state standard T Tauri star-disk system with a grid point resolution of 150x100 cells. Our disk parameters are the same as in Woitke et al. (2018) except for the radial extent R_{out}. The emitting region of molecules such as C_2H_2 in the mid-IR are limited to within 10 au (Woitke et al. 2018). Hence, we cut the radial extent of the disk to 10 au to be able to increase the spatial resolution for the inner regions. Our corresponding disk mass M_{disk} inside 10 au is only 9.495×10^{-4} $M_\odot$. We also used the canonical gas-to-dust mass ratio of 100. Figure 1 shows the physical structure of the disk model.

2.2. Thermo-chemical disk modeling

The gas temperature in PRODIMO is determined by the balance between the heating and cooling processes as listed in Woitke et al. (2009). The code uses the kinetic rate approach to obtain the chemical composition in the disk. Additional heating and cooling processes, namely, the line cooling by molecules emitting in the mid-IR such as H_2O, C_2H_2, CH_4, CO_2, NH_3, HCN, OH are included in the model (Woitke et al. 2018).

The chemical network includes the gas-phase chemistry and gas-grain desorption (thermal desorption, photo-desorption and cosmic-ray desorption) and freeze-out. The chemistry is modeled using 13 elements, namely H, He, C, N, O, Ne, Na, Mg, Si, S, Ar, Fe and PAH. Table 1 lists the elemental abundances used in all the models (Woitke et al. 2016); we used a C/O ratio of 0.457. The fiducial model uses the large DIANA chemical network consisting of 235 species, including atoms, molecules, corresponding positive ions, protonated ions and ices (Kamp et al. 2017). There are 3037 reactions in the fiducial model that largely originate from the UMIST2012 database (McElroy et al. 2013). We added two reactions from the KIDA 2014 database, which are explained in Sect. 2.3. The network has a number of specific additional reactions as mentioned in Kamp et al. (2017): X-ray chemistry (Meijerink et al. 2012; Rab et al. 2018), PAH chemistry ($C_{54}H_{18}$ is taken as a representative PAH) including adsorption and freeze out (see references in Kamp et al. 2017),

Table 1. All the elements along with their abundances used in all the models.

Elements	12 + logϵ	Abundance (relative to H)
H	12	1
He	10.98	9.64×10^{-2}
C	8.14	1.38×10^{-4}
N	7.90	7.94×10^{-5}
O	8.48	3.02×10^{-4}
Ne	7.95	8.91×10^{-5}
Na	3.36	2.29×10^{-9}
Mg	4.03	1.07×10^{-8}
Si	4.24	1.74×10^{-8}
S	5.27	1.86×10^{-7}
Ar	6.08	1.20×10^{-6}
Fe	3.24	1.74×10^{-9}
PAH	5.48	3.019×10^{-7}

collider reactions from the UMIST 2006 database and photodissociation reactions for the molecular ions (Heays et al. 2017). Photorates were calculated using the local wavelength dependent radiation field inside the disk (Kamp et al. 2010). We included a number of three body and thermal decomposition reactions taken from the STAND2020 (Rimmer & Helling 2016) listed in Appendix A. We took only those reactions from STAND2020 that have valid data for the forward direction[2]; the backward reactions for the same were not included. The H_2 formation was included following Cazaux & Tielens (2004). We go on to explore the impact of using a different H_2 formation rate (Cazaux & Tielens 2010) in Sect. 4.2.

2.3. Expanding the network for longer hydrocarbon molecules

We aim to analyse the chemical formation and destruction pathways of C_2H_2 and quantify the effect of chemistry on the C_2H_2 abundance and its mid-IR spectra. Our goal is to find chemical pathways that may be potentially missing from the existing chemical network and we study their impact on the disk. To do so, we first expand the large DIANA chemical network by adding additional longer hydrocarbon species.

We decided to restrict ourselves to the chemistry up to the most simple cyclic aromatic hydrocarbon, namely C_6H_6. We included species up till eight carbon atoms to take into account the destruction of larger hydrocarbons to form the stable C_6H_6 molecule. The negative ions are omitted except for H^-. The rule formulated in Kamp et al. (2017) which states to include the ions and protonated forms of the neutral stable closed shell species is followed. We identify the stable species as C_2H_6, C_3H_4, C_3H_6, C_4H_2, C_4H_4, C_4H_6, C_5, C_5H_2, C_5H_4, C_6, C_6H_2, C_6H_6, C_7, C_7H_2, C_7H_4, C_8, and C_8H_2. Their ions and protonated forms are added in the network except for C_4H_6. Only the protonated form of this species is added in the network because destruction reactions for $C_4H_6^+$ were unavailable in the rate databases.

In a first step, the hydrocarbon species and their isotopomers, if any, for which the destruction and formation reactions are available in the UMIST2012 database are included in the network. The network has the cyclic and linear isotopomers of C_3H denoted as C_3H and CCCH, C_3H_2 denoted as C_3H_2 and H_2CCC, and $C_3H_3^+$ denoted as $C_3H_3^+$ and CH_2CC^+, respectively. It also has both linear isotopomers of C_3H_4 denoted as CH_2CCH_2 and CH_3CCH.

The reactions for CCCH are taken from KIDA2014. Both the KIDA2014 and the UMIST2012 database do not provide the reactions for the cyclic counterpart c-C_3H^+, which might be because this species has never been detected in space. The network also misses C_6H_5 and C_6H_4 as neither of the two databases provides the destruction and formation reactions for these species. The KIDA2014 database misses $C_3H_6^+$, $C_3H_7^+$, $C_6H_6^+$, CH_2CCH_2, and UMIST misses CCCH.

This resulted in a total of 92 new hydrocarbon species added to the large chemical DIANA network. Rates for their reactions are takes from either UMIST2012 or KIDA2014. Table 2 summarizes this list and shows the stable species in bold font. Neutral hydrocarbons including the radicals can freeze on the dust grains. The adsorption energies for these neutral species are taken also from the UMIST2012 database. We assumed the same adsorption energies for both the isomers of C_3H_4 due to the lack of individual data. The enthalpy of formation at 0 K is taken from the UMIST and KIDA database, respectively. We were not able to find the heat of formation for $C_3H_6^+$, $C_4H_4^+$, $C_4H_7^+$, C_5H^+, $C_5H_2^+$, $C_5H_3^+$, C_5H_4, C_6^+, C_6H^+,$C_6H_3^+$,$C_6H_6^+$, $C_6H_7^+$, C_7H^+, $C_7H_2^+$, $C_7H_3^+$, $C_7H_4^+$, $C_7H_5^+$, CH_3C_6H, C_8^+, C_8H^+, $C_8H_3^+$, $C_8H_4^+$ and $C_8H_5^+$ in the UMIST, KIDA or NIST database. Similarly to the case of the adsorption energies, we assumed the enthalpy of formation for isotopomers to be equal for these species.

2.4. Chemical networks

We aimed to investigate the changes in the chemistry of C_2H_2 resulting from the use of different sets of rate coefficients from UMIST2012 and KIDA2014 after expanding the chemical network. We can then analyse the impact of the extended chemical network on the mid-IR spectra from the disks. To build up our understanding, we used a series of models.

Our fiducial model uses the large DIANA chemical network with 235 species (Kamp et al. 2017), plus the set of three body and thermal decomposition reactions listed in Appendix A. The heating and cooling processes that determine the gas temperature are intertwined with the chemistry. Hence, we decided to fix the physical structure of the disk (gas, dust temperatures and densities) to that of the fiducial model for all subsequent models. Only the chemical concentrations were recalculated. This allows us to isolate the effect of chemical rates on the species abundances, the line emitting regions of the molecules, and the mid-IR line fluxes.

Each model has a barrier-less charge exchange and a dissociative recombination formation reaction for C_2H_2 taken from the KIDA2014 database:

$$C + C_2H_2^+ \rightarrow C_2H_2 + C^+ \quad (1)$$

$$C_3H_3^+ + e^- \rightarrow CH + C_2H_2. \quad (2)$$

These reactions[3] constitute a dominant formation pathway of C_2H_2 when using KIDA2014 and were thus added in all the models.

Table 3 summarises the different models that we use in this work. The chemical database and the size of the chemical network are varied in the models. Model 2 uses the large DIANA chemical network with the rates calculated using the rate coefficients provided by the KIDA2014 database. Models 3 and 4

[2] A+B+M → C+D+M, reverse of such a reaction is not added.

[3] All the reactions referenced are from within the text.

Table 2. All the hydrocarbons present in the extended chemical network.

C	2C	3C	4C	5C	6C	7C	8C
CH	$\mathbf{C_2}$	$\mathbf{C_3}$	$\mathbf{C_4}$	$\mathbf{C_5}$	$\mathbf{C_6}$	$\mathbf{C_7}$	$\mathbf{C_8}$
CH_2	C_2H	C_3^+	C_4^+	C_5^+	C_6^+	C_7^+	C_8^+
CH_3	$\mathbf{C_2H_2}$	C_3H	C_4H^+	C_5H	C_6H	C_7H	C_8H
$\mathbf{CH_4}$	C_2H_3	C_3H^+	C_4H	C_5H^+	C_6H^+	C_7H^+	C_8H^+
CH^+	$\mathbf{C_2H_4}$	$\mathbf{C_3H_2}$	$\mathbf{HC_4H}$	$\mathbf{C_5H_2}$	$\mathbf{C_6H_2}$	$\mathbf{C_7H_2}$	$\mathbf{C_8H_2}$
CH_2^+	C_2H_5	$C_3H_2^+$	C_4H_3	$C_5H_2^+$	$C_6H_2^+$	$C_7H_2^+$	$C_8H_2^+$
CH_3^+	C_2^+	$C_3H_3^+$	$\mathbf{CH_2CHCCH}$	$C_5H_3^+$	$C_6H_3^+$	$C_7H_3^+$	$C_8H_3^+$
CH_4^+	C_2H^+	CCCH (l-C_3H)	$\mathbf{CH_2CHCHCH_2}$	$\mathbf{CH_3C_4H}$	$C_6H_4^+$	$C_7H_4^+$	$C_8H_4^+$
CH_5^+	C_2H2^+	H_2CCC (l-C_3H_2)	$C_4H_2^+$	$CH_3C_4H^+$	$C_6H_5^+$	$C_7H_5^+$	$C_8H_5^+$
CH#	$C_2H_3^+$	CH_2CCH	$C_4H_3^+$	$C_5H_5^+$	$\mathbf{C_6H_6}$	$\mathbf{CH_3C_6H}$	C_8#
CH_2#	$C_2H_4^+$	$\mathbf{CH_3CCH}$	$C_4H_4^+$	C_5#	$C_6H_6^+$	C_7#	C_8H#
CH_3#	$C_2H_5^+$	$\mathbf{CH_2CCH_2}$	$C_4H_5^+$	C_5H#	$C_6H_7^+$	C_7H#	C_8H_2#
CH_4#	$\mathbf{CH_3CH_3}$	$\mathbf{CH_3CHCH_2}$	$C_4H_7^+$	C_5H_2#	C_6#	C_7H_2#	
	$CH_3CH_3^+$	CH_2CCH^+	C_4#	CH_3C_4H#	C_6H#	CH_3C_6H#	
	$C_2H_7^+$	$C_3H_4^+$	C_4H#		C_6H_2#		
	C_2#	$C_3H_5^+$	HC_4H#		C_6H_6#		
	C_2H#	$C_3H_6^+$	C_4H_3#				
	C_2H_2#	$C_3H_7^+$	CH_2CHCCH#				
	C_2H_3#	C_3#	$CH_2CHCHCH_2$#				
	C_2H_4#	C_3H#					
	C_2H_5#	C_3H_2#					
	CH_3CH_3#	CCCH#					
		H_2CCC#					
		CH_2CCH#					
		CH_3CCH#					
		CH_2CCH_2#					
		CH_3CHCH_2#					

Notes. The species in gray were present in the large DIANA chemical network (and are present in all models). The species in black are added to this network. All these species are present in model 5. All the species except the underlined ones are present in models 3 and 4. The stable species are marked in bold. The ices of neutral species are represented by #.

Table 3. Models used in this paper specifying the details of the chemical network.

Model #	Database	# of species	# of reactions
Fiducial	UMIST2012	235	3036
Model 2	KIDA2014	235	3072
Model 3	UMIST2012	320	4004
Model 4	KIDA2014	320	4150
Model 5	UMIST2012	327	4121

use the new extended chemical network consisting of all the species in Table 2, except the underlined ones, along with the rate coefficients for reactions primarily taken from UMIST2012 and KIDA2014, respectively. They share the same species to facilitate the comparison between the two databases. This is why they lack seven species, namely $C_3H_6^+$, $C_3H_7^+$, $C_6H_6^+$, $CH_2CCH_2(C_3H_4)$ and its corresponding ice CH_2CCH_2#, and CCCH and its corresponding ice CCCH#[4]. The databases are not complete in providing all the required reactions and species. For example, the UMIST2012 database clubbed c-$C_3H_2^+$ and l-$C_3H_2^+$ together as $C_3H_2^+$ which is used in model 3. We therefore use c-$C_3H_2^+$ from the KIDA2014 database as its counterpart in model 4.

Model 5 has the missing seven species included and uses the UMIST2012 database and a few selected reactions added from the KIDA2014 database for CCCH. Model 5 thus presents the complete extended chemical network. Model 5 also includes the following dissociative recombination reaction with electrons:

$$C_4H_3^+ + e^- \rightarrow C_2H + C_2H_2. \quad (3)$$

with the rate coefficient taken from the KIDA2014 database.

3. The hydrocarbon chemistry

The abundance of C_2H_2 in the fiducial model is shown in Fig. 2. C_2H_2 resides in a thin surface layer and two larger reservoirs in the midplane around 0.1 au and 2 au. This general qualitative structure of the C_2H_2 abundance is the same in all the models no matter what size of network or database we use; and only the radial extent changes slightly.

To understand the formation of C_2H_2 in our disk model, we have chosen three representative grid points from the three reservoirs shown as white circles in Fig. 2. Grid point 1 is the representative point for surface chemistry that lies around the

[4] # represents ices of the corresponding species.

Table 4. Properties of the grid point for which the chemistry was analysed in various models.

Point	r, z (au)	T_{gas} (K)	T_{dust} (K)	A_v^{rad}	A_v^{ver}	$n_{<H>}$ (cm^{-3})	χ	Remark	Reservoirs in fiducial model
1	1.41, 0.30	300	230	1.10	0.021	5.6×10^9	3.3×10^5	Surface layer	H_2,He,O,C,CO
2	1.79, 0.19	85	85	3200	13	1.3×10^{12}	0	Outer midplane	H_2,He,CO,C_3H_2#
3	0.1, 0.0085	480	480	1700	62	2.2×10^{14}	0	Inner midplane	H_2,He,CH_4,H_2O,

Notes. Location describes the radial and vertical direction in the disk model. $n_{<H>}$ is the particle density of H, A_v^{rad} and A_v^{ver} are the radial and vertical visual extinction, χ is the UV radiation field at that location in units of drain field. The final column mentions the main form of C, H, He, O in the reservoir in the surface layers in the fiducial model.

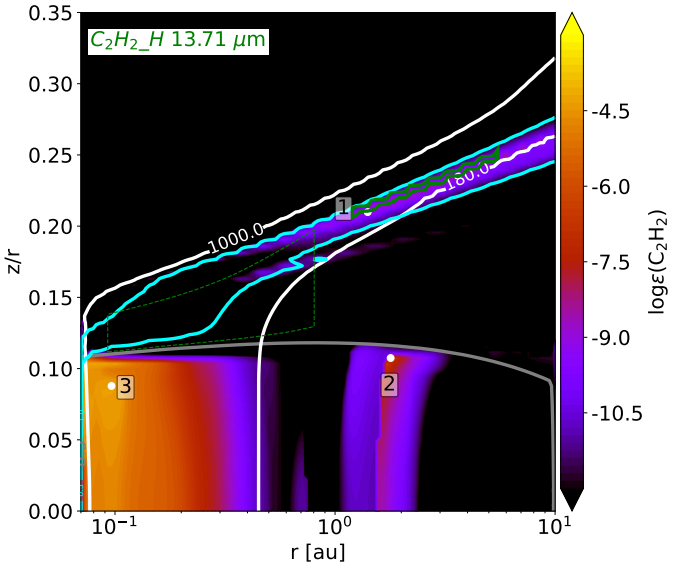

Fig. 2. Abundance of C_2H_2 with respect to $n_{(H)}$ obtained from the fiducial disk model. The white lines show the gas temperature contours for 180 K and 1000 K The gray contour depicts A_V = 8.5. The green dotted line shows the region from which 50% of the continuum emits at ~13.7 μm (representative of the ν_5 fundamental band). The green solid line shows the region where 50% of the flux is emitted by C_2H_2 at 13.7 μm. The white dots indicate the grid points for which the chemistry is subsequently analysed in detail. The cyan contours depict where 20 and 99% of hydrogen is in the form of H_2.

emitting region of the C_2H_2 transition at 13.706 μm above the continuum emitting surface at 13.7 μm. This particular transition is chosen as it has the highest flux in the fiducial model. Grid points 2 and 3 reside in regions of maximum abundance of C_2H_2 in the two reservoirs in the midplane. Table 4 summarises the properties of the locations that were analysed. The typical abundance in the models in the surface layers (grid point 1) and the regions beyond $r \leq 1$ au (grid point 3) is of the order of 10^{-9} and 10^{-5}, respectively. The surface layer is confined to a region where the abundance of H_2 is higher than ~0.05, the abundance of H is higher than ~0.0019 and the abundance of C is of the order of ~10^{-6}. The two regions in the midplane are confined by the absence of electrons. In regions with an electron abundance of $\geq 10^{-11.5}$, the abundance of C_2H_2 is low ($\leq 10^{-12}$). In the second reservoir around 2 au, O is depleted from the gas as it forms H_2O ice. The gas then becomes C-rich and this gives rise to carbon chemistry.

First, the chemistry of C_2H_2 at grid point 1 in the surface layer is analysed. The major formation and destruction pathways of C_2H_2 in the fiducial model are shown in Fig. 3. Carbon, being the key ingredient of any hydrocarbon chemistry, is unlocked by the photodissociation of CO by UV photons. It can also be unlocked as C^+ when He^+ dissociates CO. He^+ is produced either by X-rays or cosmic rays, depending on which one is dominant in the surface layers. There are two pathways forming C_2H_2 as shown in the two color-shaded regions of Fig. 3: the neutral-neutral pathway (purple) and the ion-molecule pathway (orange). The formation of C_2H_2 via the neutral-neutral pathway proceeds via the hydrogenation of C. The reaction of H_2 with C forms CH_2 which dissociates to form CH. The reaction of C with H also forms CH. These reactions are barrier less and so depend only on the abundances of H, H_2 and C. Once CH is formed, it can form C_2 via the addition of neutral C. This is followed by abstraction of H to form C_2H and finally C_2H_2. The ion-molecule pathway proceeds through hydrogen addition. Starting from C^+, this leads to the formation of CH_3^+ via CH^+. The addition of neutral C then forms C_2H^+. Again, as these reactions are barrier-less, the availability of neutral C is the limiting factor here. Thus for both pathways, the availability of C, H and H_2 is pivotal in deciding the formation route of C_2H_2 in the surface layers. This fundamental chemistry is valid for all the models. The pathways leading to C_2H_2 via C and C^+ are same in all the models. The rates of the reactions differ because of the differences in the abundances and the rate coefficients between the two databases.

C_2H_2 is destroyed to form higher hydrocarbons via the addition of C in the fiducial model. An example is the formation of C_3H. The other destruction path is C_2H_2 photodissociation to C_2H.

In the fiducial model, at grid point 2, we find the ion-molecule chemistry to dominate. The most important pathways to forming C_2H_2 are:

$$C_3H_2 + C_2H_3^+ \rightarrow C_2H_2 + C_3H_3^+, \quad (4)$$

$$C_3H_3^+ + e^- \rightarrow CH + C_2H_2, \quad (5)$$

$$C_3H + C_2H_3^+ \rightarrow C_2H_2 + C_3H_2^+. \quad (6)$$

These formation pathways are not relevant in the surface layers. As the surface layers are UV dominated, C_3H_2 is photodissociated to C_3H instead of forming C_2H_2. Figure 4 shows the difference in the abundances for C_2H_2 in all our models which we discuss in the following subsections.

3.1. The extended hydrocarbon chemistry using the UMIST database

In model 3, we add the hydrocarbon species that are common to the UMIST2012 and the KIDA2014 rate database as shown

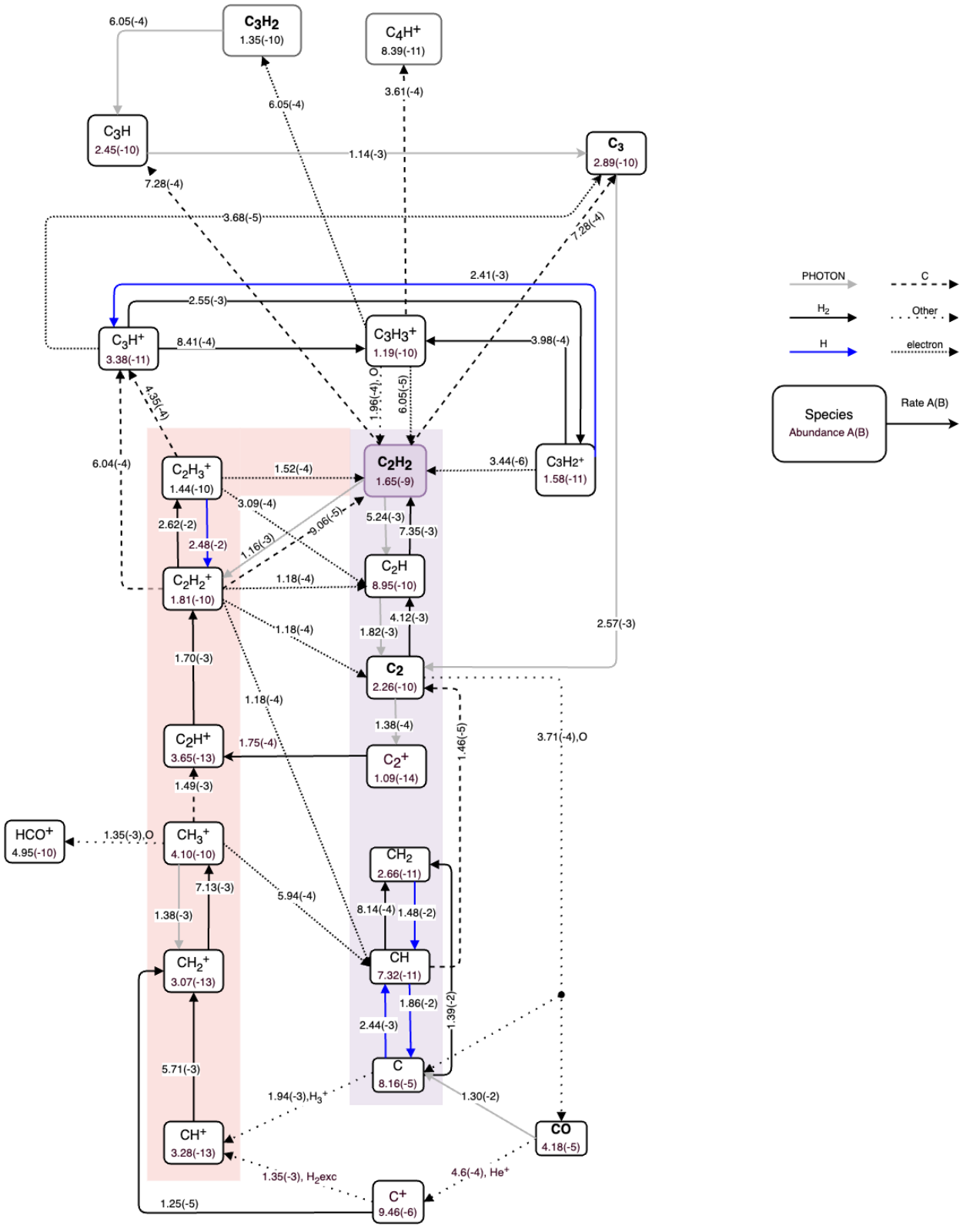

Fig. 3. Chemical network centered around C_2H_2 depicting the dominant formation and destruction pathways of parent molecules for the fiducial model in the surface layers (grid point 1). It includes large DIANA chemical species and uses the UMIST2012 rate coefficients. The rates are indicated on the paths. The A(B) notation represents $A \times 10^B$. The species abundance in the surface layer in the fiducial model for a grid point is noted below the species.

in Table 2. Model 3 only uses reactions from the UMIST2012 rate database. The new C_2H_2 abundances are shown in Fig. 4 (lower left panel). To understand the differences in abundance of C_2H_2 between the fiducial model and this model 3, Fig. 5 highlights the differences in the pathways described in the previous section.

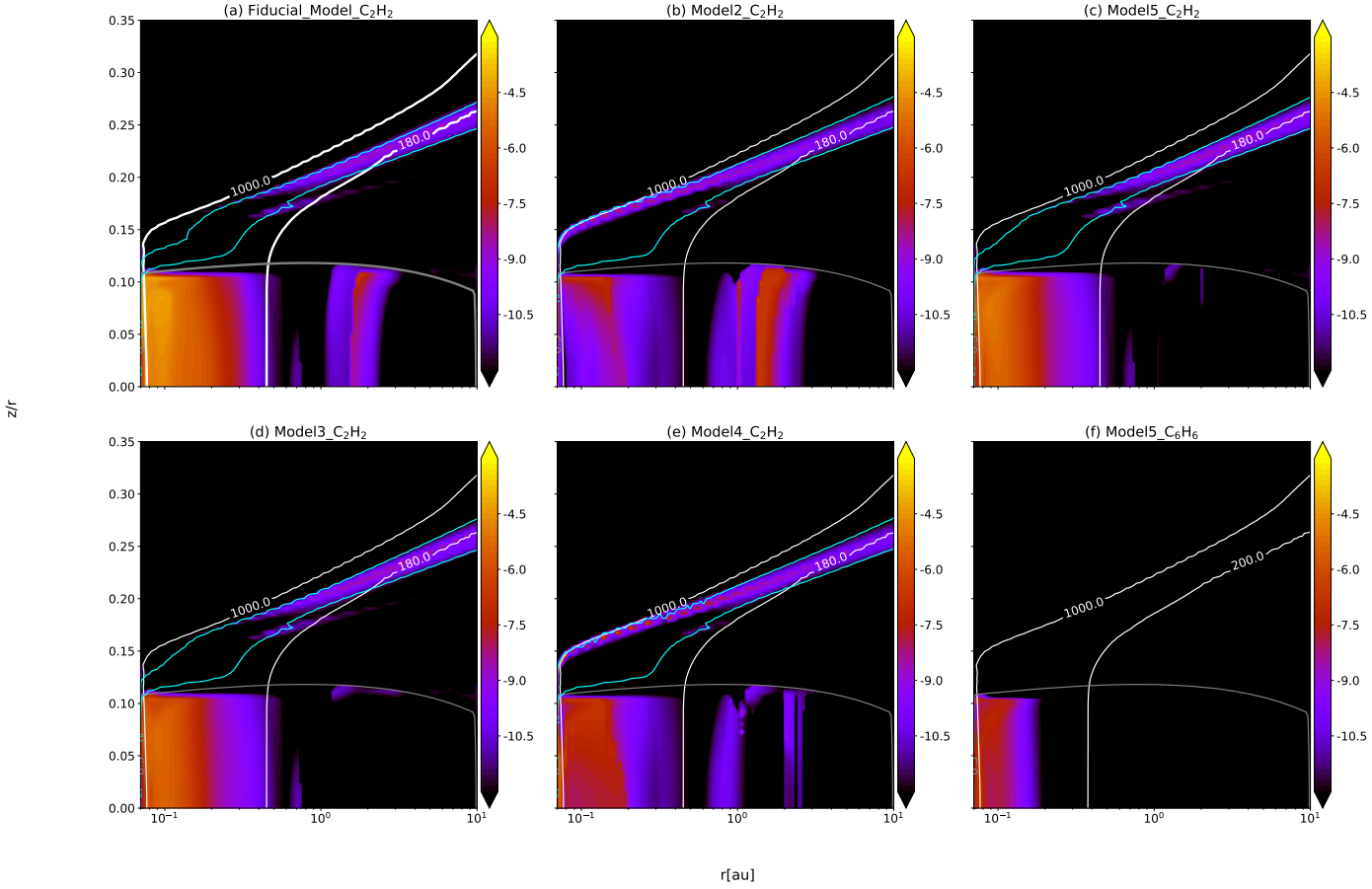

Fig. 4. Abundances of species C_2H_2, C_6H_6 in different models. The gray contour corresponds to A_V = 8.5. The temperature contours of 1000 K and 180 K are shown in white. The cyan contours represent where 20 and 99.8% of hydrogen is in the form of H_2.

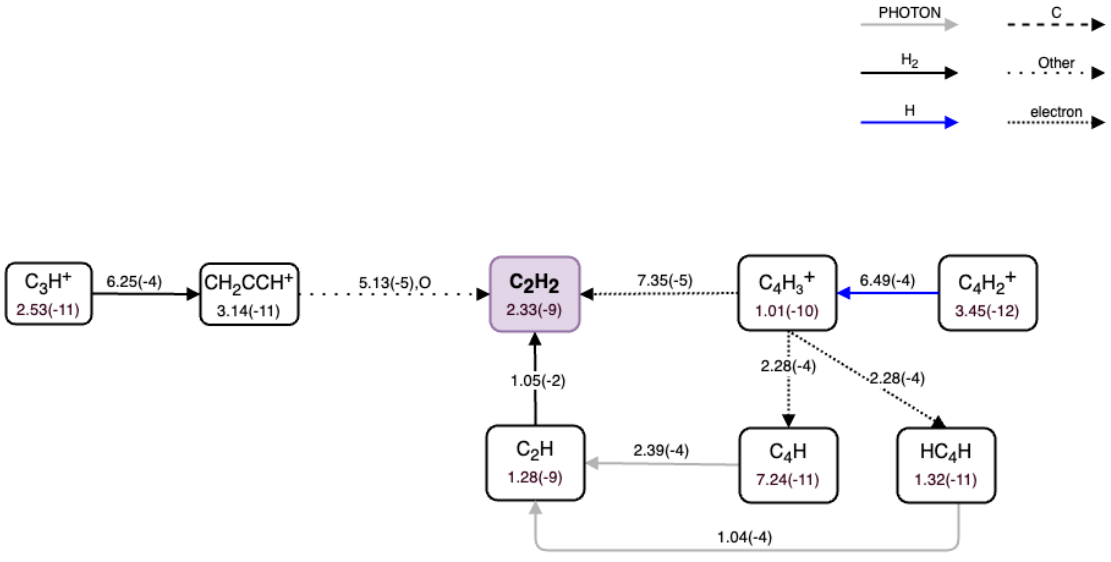

Fig. 5. Zoomed-in chemical network showing the formation pathways that become active after adding the longer hydrocarbons. The abundances and rates correspond to model 3 (extended hydrocarbon network using the UMIST2012 rate database). This also highlights the major differences in the formation pathways of C_2H_2 between Figs. 3 and 6.

In the surface layers, namely, grid point 1, the total formation rate of C_2H_2 increases by ∼41% in model 3 relative to the fiducial model. This increase is due to the new pathways that are active now, but which were missing from the fiducial model. Figure 5 shows these new pathways that form C_2H_2.

The other difference is the formation of C_2H via breaking down larger hydrocarbons in model 3. For example, the

following two reactions were absent in the fiducial model

$$HC_4H + h\nu \rightarrow C_4H + H \quad (7)$$

$$C_4H + h\nu \rightarrow C_2H + C_2. \quad (8)$$

Then, C_4H dissociates to smaller hydrocarbon molecules such as C_2H and C_2. These two molecules are steps in the formation of C_2H_2 as seen in Fig. 3. Enhancing their abundances will propagate and lead to a higher abundance of C_2H_2.

The abundance of C_2H_2 in the outer midplane (i.e. grid point 2) drops by six orders of magnitude in model 3 with respect to the fiducial model (Fig. 4). Due to the presence of longer hydrocarbons and their corresponding more stable ices, the carbon is bound in the ices of longer hydrocarbons. The most abundant ice at this location is benzene ice C_6H_6#. The gas-phase longer hydrocarbon species are concentrated in the inner midplane regions roughly within 0.5 au at T_{gas} higher than ~200 K.

In the inner midplane (i.e. grid point 3), the total formation rate of C_2H_2 decreases by an order of magnitude in model 3 compared to the fiducial model resulting in a decrease in abundance by an order of magnitude. The dominant formation pathway in the fiducial model is

$$C_2H_3 + H \rightarrow C_2H_2 + H_2. \quad (9)$$

This reaction is exactly balanced by the destruction of C_2H_2 via a three-body reaction,

$$C_2H_2 + H + M \rightarrow C_2H_3 + M, \quad (10)$$

in model 3 making the thermal decomposition of CH_2CCH by M (where M may be H, He, or H_2) the dominant formation pathway. As we go deeper in the disk (r = 0.07au, z = 0.007au, T_{gas} = 1100 K and $n_{<H>} = 2.3 \times 10^{14} cm^{-3}$), we find that these major formation pathways are balanced by neutral-neutral or three-body destruction pathways making secondary species such as H_2O important in forming C_2H_2.

The neutral-neutral destruction reaction of C_2H_2,

$$C_2H_2 + CH_2 \rightarrow CH_2CCH + H, \quad (11)$$

is favoured over cosmic ray induced photodissociation of C_2H_2 to form C_2H; this reaction is missing from the fiducial model. This again highlights the importance of adding higher hydrocarbons to determine more reliable C_2H_2 abundances.

3.2. Role of isomers in the extended hydrocarbon network

We compared models 2 and 4 (i.e. the large DIANA and extended chemical network) using the KIDA2014 rate database, respectively. We found two new pathways which are reaction (3) and the dissociative recombination of CH_2CCH^+ with e^- forming C_2H_2 in model 4 (at point 1, Fig. B.2). These are the new species added in the extended network. The dissociative recombination reaction of C_3H_2 with e^- becomes less important in model 4. This is due to a lowered abundance of $C_3H_2{}^+$. Its formation proceeds via:

$$H_2 + C_3H^+ \rightarrow C_3H_3{}^+ + h\nu, \quad (12)$$

$$H + C_3H_3{}^+ \rightarrow C_3H_2{}^+ + H_2, \quad (13)$$

in model 2. In the extended network, the first step can branch to two isomers, $C_3H_3{}^+$ (c-$C_3H_3{}^+$) and CH_2CCH^+ (l-$C_3H_3{}^+$), thus lowering the abundance of $C_3H_3{}^+$ and, consequently, lowering the abundance of $C_3H_2{}^+$. However, the decrease in this rate is compensated by the two new pathways above, overall resulting in an increase of ~40% in the abundance of C_2H_2 at grid point 1 in model 4.

One of the major formation pathways in both models at grid point 3 is:

$$C_2H_3{}^+ + H_2O \rightarrow C_2H_2 + H_3O^+. \quad (14)$$

The thermal decomposition of CH_2CCH by M and dissociative recombination of $C_5H_5{}^+$ with e^- added to the production of C_2H_2. Both were missing from the DIANA chemical network, thus increasing the C_2H_2 abundance by two orders of magnitude in the inner disk midplane region (point 3).

3.3. Comparison between the UMIST and KIDA rate databases

Figure 4 shows the difference in the radial extent of the surface layer of C_2H_2 in models using the UMIST2012 and the KIDA2014 rate database. We traced this back to the layer with high H_2 abundances extending down to smaller radii in models using the KIDA2014 database. The chemical pathways displayed in Fig. 3 show that H_2 is crucial in the formation of C_2H_2. Comparing two models using the same chemical network but different rate databases (models 3 and 4), the vertical height at which H/H_2 transition occurs is higher by ~0.005 au at the radial distance of 1 au in model 4 (KIDA2014) compared to model 3 (UMIST2012). Models making use of the UMIST2012 database (fiducial and model 2) have a higher destruction rate of H_2. There is more destruction of H_2 by atomic oxygen in the UMIST2012 model compared to the KIDA2014 model due to different rate coefficients for the reaction:

$$O + H_2 \rightarrow H + OH. \quad (15)$$

The C_2H_2 abundance at grid point 3 for model 2 is lower compared to the fiducial model as seen in Fig. 4. In the fiducial model, C is locked in C_2H_2, while in model 2 more of the C is instead in CH_4 at the inner midplane (grid point 3). We attribute this difference to missing reactions and different rate coefficients given in the databases. The reaction

$$CH_3 + C_2H_3 \rightarrow C_2H_2 + CH_4 \quad (16)$$

is missing from the KIDA2014 database, but it is one of the dominant destruction reactions for C_2H_3 and the dominant formation reaction for CH_4 and C_2H_2 when using UMIST2012 (fiducial model). The following dominant formation reaction in the fiducial model,

$$C_2H + H_2 \rightarrow C_2H_2 + H \quad (17)$$

has a barrier of 1300 K in KIDA2014 but only 130 K in UMIST2012, which explains the lower rate in model 2. Another important species contributing to the formation of C_2H_2 is $C_2H_3{}^+$. This molecular ion is formed via the reaction

$$C_2H_2{}^+ + H_2 \rightarrow C_2H_3{}^+ + H, \quad (18)$$

which is a barrier-less reaction in UMIST2012 but has an activation energy of 2000 K in KIDA2014. The combination of these differences lead to a lower abundance of C_2H_2 in model 2 at grid point 3 when compared to the fiducial model.

Table 5. Species missing in the databases.

Only in UMIST2012	Only in KIDA2014
$C_3H_6^+$	CCCH
$C_3H_7^+$	
$C_6H_6^+$	
CH_2CCH_2	

Notes. Stable species are marked in bold.

3.4. Benzene formation

Benzene is confined to the inner midplane below $r \leq 0.2$ au and a z/r of ∼0.1. It also appears in a narrower radial region in model 4 (KIDA2014, extended hydrocarbon chemistry). To find the dominant formation and destruction pathways in models, we analysed the chemistry in the inner midplane, at $r = 0.086$ au and $z/r = 0.07$, with $T_{\rm gas} = T_{\rm dust} = 570$ K, in an optically thick region with $A_{\rm V}^{\rm ver} = 150$ and $A_{\rm V}^{\rm rad} = 2400$ and $n_{<\rm H>} = 5.6 \times 10^{14}$cm^{-3}. We chose this point as it has the maximum abundance of benzene in model 5 (final extended chemical network). The network might be missing some reaction as the databases are not complete in hydrocarbons with six C atoms such as C_6H_4, C_6H_5 etc. The pathway to form benzene is via CH_4 and C_2H_2. In model 3 (using UMIST2012), the dominant pathway of formation is

$$CH_4 + C_5H_2^+ \rightarrow C_6H_5^+ + H, \quad (19)$$

contributing ∼90% to the total formation rate, followed by

$$C_2H_2 + C_4H_3^+ \rightarrow C_6H_5^+ + h\nu, \quad (20)$$

contributing only ∼5%. Then, $C_6H_5^+$ reacts further with H_2 to form $C_6H_7^+$, which subsequently recombines with an electron to form benzene:

$$H_2 + C_6H_5^+ \rightarrow C_6H_7^+ + h\nu, \quad (21)$$

$$C_6H_7^+ + e^- \rightarrow C_6H_6 + H. \quad (22)$$

Model 4 (KIDA2014) also follows the same formation scheme as explained above. However, the abundance of benzene at this location in model 4 is of the order of 10^{-14}, but even when analysing the region with the highest abundance (10^{-10}) we find the same formation mechanism that then leads to C_6H_6 via dissociative recombination (reaction (22)).

3.5. The final hydrocarbon network

Based on what we learned from the previous comparisons, we compiled the final chemical network which has 327 species in total combining the large DIANA network with 235 species and the 92 additional hydrocarbons from Table 5. The leading database is UMIST2012 as it has more species than KIDA2014 and we added a few reactions picked from the KIDA2014 database as described in Sect. 2.3. The network includes the three body and thermal decomposition reactions as mentioned in Appendix A.

The basic formation and destruction pathways of C_2H_2 remain the same as described in Sect. 3.1. Figure 6 details the chemical pathways in the surface layers of the disk. The dominant reactions forming C_2H_2 are reactions (1), and the following:

$$C_2H + H_2 \rightarrow C_2H_2 + H, \quad (23)$$

$$C_2H_3^+ + e^- \rightarrow C_2H_2 + H. \quad (24)$$

These were also the dominant formation reactions in model 3 for the surface layers. The addition of new hydrocarbons changes the abundances of C_2H_2 in the inner and outer midplane by two and seven orders of magnitude, respectively, compared to the fiducial model for the reasons explained in previous sections. However, it does not affect the C_2H_2 abundances in the surface layers much (increasing only by a factor of ∼1.5).

In the final network, the reaction of H_2 with $C_6H_5^+$ leads to $C_6H_7^+$, which recombines with an electron to form benzene (see reactions (22) and (21)). Reaction (19) contributes ∼83% and reaction (20) contributes ∼16% to the total formation rate of $C_6H_5^+$. Hence, both CH_4 and C_2H_2 contribute to the formation of C_6H_6 with the route through CH_4 being the dominant one. Figures 7 and 8 show the effect of adding complex hydrocarbons and highlights how carbon chain length changes throughout the disk. The shades of blue and red corresponds to the single C and two C atom-bearing species. The diversity in the ices also increase on using the extended chemical network. This network will be used for the remainder of the paper.

4. Mid-IR spectra

The extended hydrocarbon chemistry has an effect on the chemical abundances, especially with respect to C_2H_2. We study here whether this has an impact on the mid-infrared spectra emitted from the disk. We use the escape probability method, which yields vertically emitted total line fluxes (Woitke et al. 2009) and FLiTs developed by Michiel Min (Woitke et al. 2018). FLiTs does a full line radiative transfer including the dust continuum and line opacity overlap. We used HITRAN 2009 (Rothman et al. 2009) as our spectroscopic database. The rules for selecting the line transitions were taken from Woitke et al. (2018).

Figure 9 shows the line flux for C_2H_2 calculated using the escape probability method and FLiTs convolved to a resolution of 3000 appropriate for JWST. The weak lines at ∼14 µm have higher fluxes using the escape probability method compared to FLiTs (see residuals in Fig. 9). The escape probability treatment do not take into account absorption by the continuum which can be an issue for molecules emitting from relatively low heights in the disk. The escape probability produces a higher (by a factor 2) integrated C_2H_2 (11.8–16.22 µm) flux relative to FLiTs as shown in Fig. 9. In the following, we used FLiTs to calculate the spectra.

4.1. Implication on mid-IR spectra

Figure 10 shows the flux emitted by C_2H_2 for the model with the expanded hydrocarbon chemistry (model 5) and the one using the large DIANA chemical network (fiducial model). The total integrated flux in model 5 is higher by 10% relative to the fiducial model. This increase is solely because of the use of the expanded chemical network as we fixed the gas temperature of the disk. The peak fluxes produced in model 5 are ∼0.6mJy at $R = 3000$ and ∼0.33 mJy at $R = 600$. The peak flux for C_2H_2 in T Tauri disks as observed by *Spitzer* is ∼20 mJy at a $R = 600$. We find that using an extended chemical network cannot enhance C_2H_2 emission to the typical flux level of mid-infrared observations of TTauri disks. So, the next step is to use this large hydrocarbon chemistry network in an extensive investigation to identify the key physical parameters and processes (e.g. UV radiation, disk mass etc.) that are able to reproduce the observed C_2H_2 fluxes.

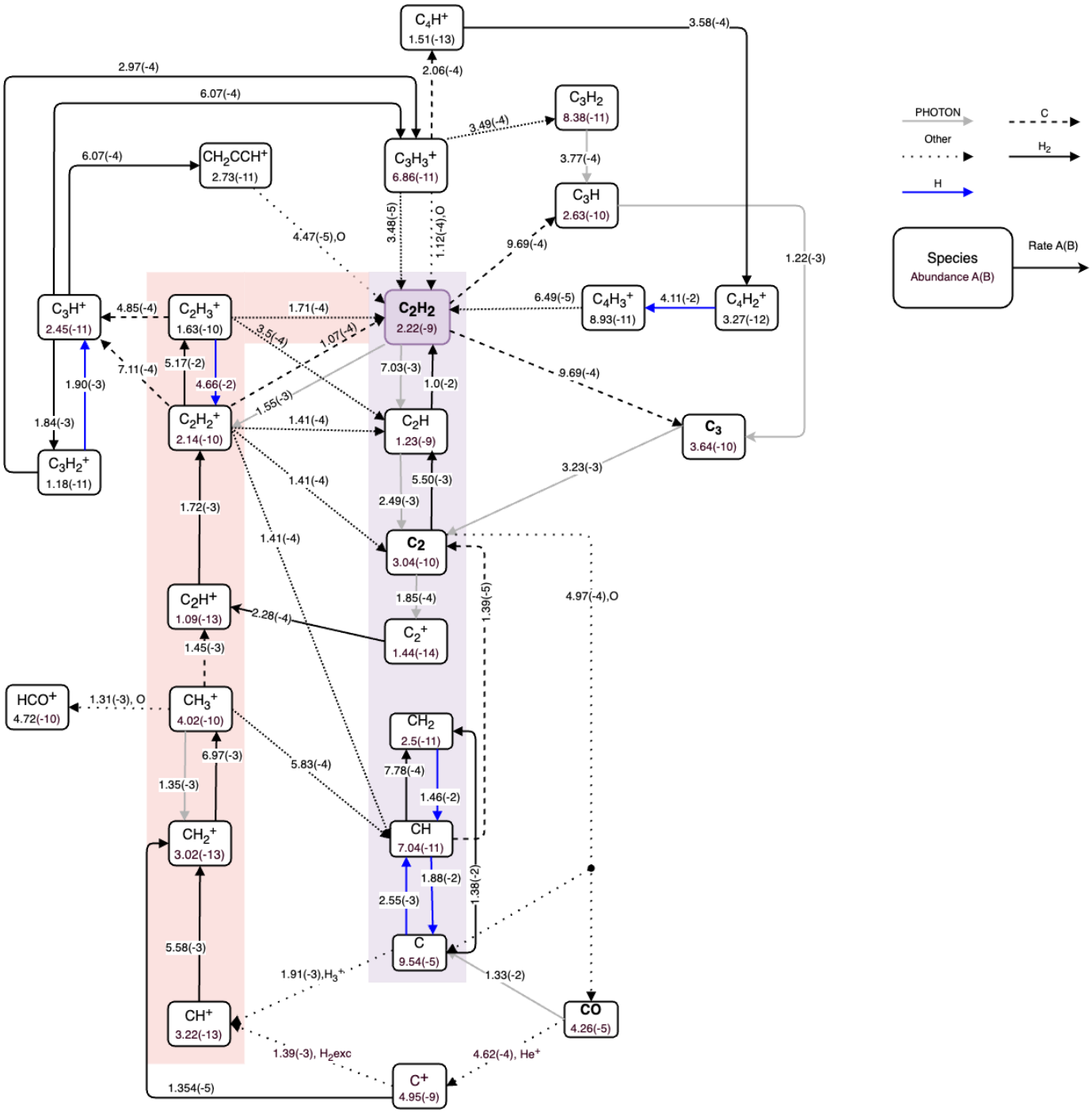

Fig. 6. Chemical network for the surface layers for model 5 (final hydrocarbon network) centered around C_2H_2.

The integrated line flux for C_2H_2 is a factor of 3 higher in model 4 (KIDA2014), compared to model 3 (UMIST2012), which both have the same chemical network (i.e. equal number of species). The difference arises from the different rate coefficients in the two databases. This leads to the molecular layer being shifted radially inwards in model 4 and being ~50% more vertically extended (see Fig. 11, also Sect. 3.3). As a result, the C_2H_2 abundance and the abundance-weighted gas temperature is higher in model 4 by ~53% (see Fig. 12), which leads to the higher line fluxes (by a factor of 3).

As seen in Fig. 2, in our fiducial model (TTauri disk model, power law surface density profile with a sharp inner edge), only the surface layers contribute towards the mid-IR emission. However, Woitke et al. (2023) propose a disk model for EX Lupi with a steadily increasing surface density at the inner rim. This fits the spectral energy distribution, the overall shape of the mid-IR spectra observed by JWST, and the observed molecular features and its characteristics, such as emitting area and gas temperatures. In their model, they find a high abundance of C_2H_2 in the O-rich gas around the inner rim, caused by X-ray irradiation. This region corresponds to our inner midplane (grid point 3) reservoir of C_2H_2. This recent work shows that for models with a different physical structure, the inner regions (grid point 3) can also contribute to the mid-IR emission.

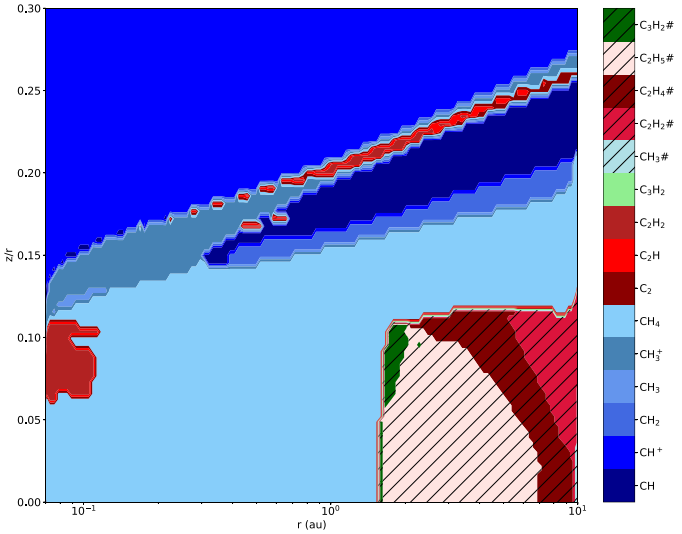

Fig. 7. Distribution of the most abundant hydrocarbons in the fiducial disk model (large DIANA chemistry and UMIST2012 rate coefficients). Each grid point depicts the most abundant hydrocarbon at that location. We do not consider C or C^+ when finding the abundant hydrocarbons.

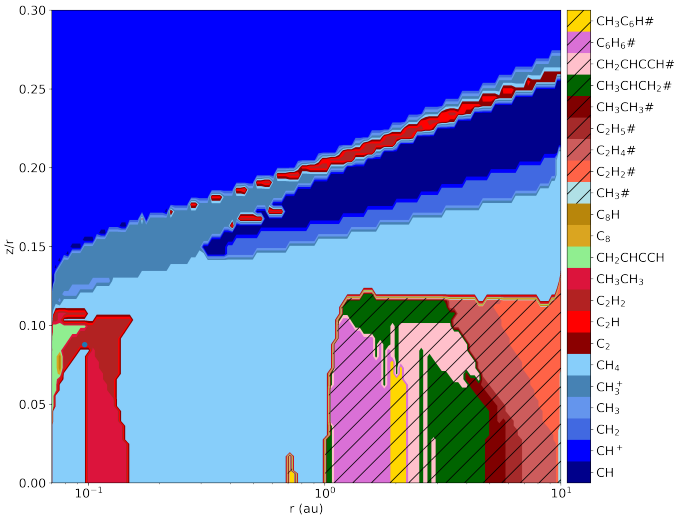

Fig. 8. Distribution of the most abundant hydrocarbons in model 5 (final extended chemical network).

4.2. The effect of H_2 formation on C_2H_2

In Sect. 3, we show that the H/H_2 transition is important for the abundance of C_2H_2 and in Sect. 4.1, we show that this affects also the flux emitted from this molecule. Hence, the formalism of how H_2 forms may affect the abundance of C_2H_2 in the disk surface layer.

To investigate this, we compared the two approaches of H_2 formation described in Cazaux & Tielens (2004, 2010). In cold regions, the formation of H_2 from physisorbed H dominates whereas in warm regions, the formation of H_2 can also proceed via chemisorbed H. Figure 13 shows how the height of the H/H_2 transition (z/r) shifts upwards by 0.005 au at r = 1 au when using an improved treatment of mobility of H atoms on grain surfaces at warmer temperatures. Model H_2Cazaux (in Figs. 12 and 11) show the effect on the gas temperature, C_2H_2 abundance, and the emitting area of using different databases and the chemical networks. Model H_2Cazaux used extended chemical network

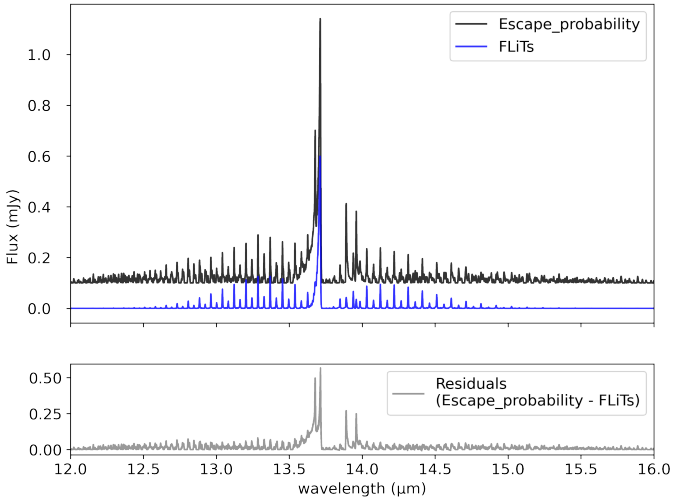

Fig. 9. Flux emitted by C_2H_2 in model 5, convolved at a spectral resolution of $R = 3000$ calculated using the escape probability method (black) and using the FliTs code (blue). The bottom panel shows the differences in the line flux between the two methods.

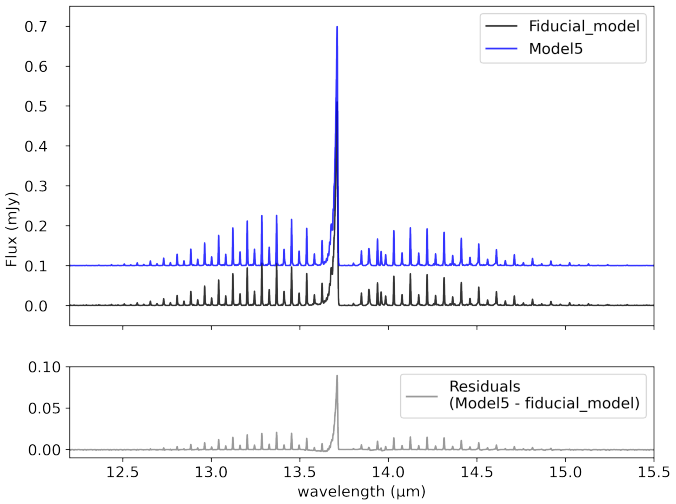

Fig. 10. C_2H_2 flux using the FLiTs code for the model with large DIANA network (fiducial model) and the extended hydrocarbon chemistry (model 5) convolved to the spectral resolution of $R = 3000$. The bottom panel shows the difference in the line flux between the two models.

with the UMIST2012 rate database. The peak flux emitted by C_2H_2 at ~13.7 μm (Q branch) increases by a factor of ~2 (escape probability method) when using the Cazaux & Tielens (2010) formalism. The increase in flux can be attributed to the increased gas temperature of the line emitting region as shown in Fig. 12 when compared to model 5. Also in this case, the surface layer of C_2H_2 extends radially inwards into the inner disk regions as warm temperatures promote the chemisorption channel for H_2 formation.

5. Discussion

We studied various pathways leading to the larger hydrocarbons in protoplanetary disks, specifically C_2H_2. We isolate the major formation and destruction pathways for C_2H_2 and C_6H_6 and their differences on the basis of whether the UMIST2012 or KIDA2014 rate databases were used. We studied the effect of the

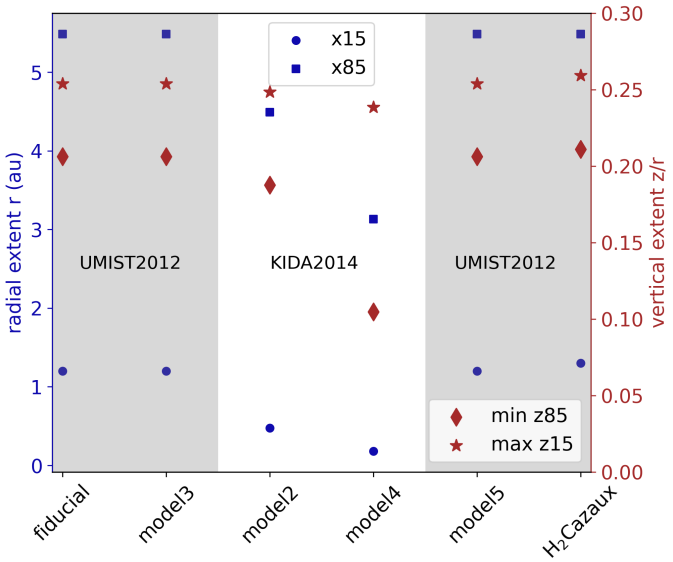

Fig. 11. Effect on the emitting region of the C_2H_2 at 13.71 µm line due to different chemical networks and the rate databases. The left and right axes depict the maximum radial and vertical extent of the emitting region. x15, x85, z15(r) and z85(r) denote the radii and heights at which 15 and 85% of the line flux have originated, respectively. Min z85 and max z15 indicate the maximum vertical extent (z/r) of the region. The gray background is used to highlight the models using the UMIST2012 database, while the white background pertains to models using the KIDA2014 database.

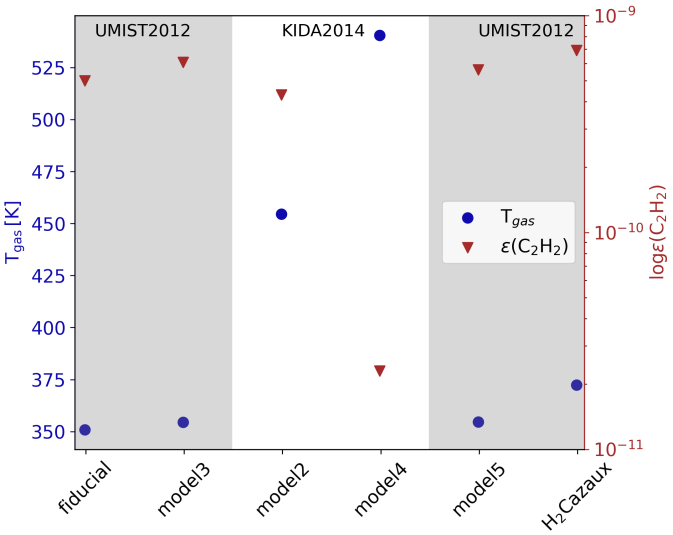

Fig. 12. Gas mass weighted abundance of C_2H_2 (brown) and C_2H_2 abundance weighted gas temperature (blue) of the emitting region of C_2H_2 at 13.71 µm for all the models. The gray background depicts the models using the UMIST2012 database and white the ones using the KIDA2014 database.

H/H_2 transition layer on the surface layers of C_2H_2 when using different H_2 formation formalisms. We compared the hydrocarbon chemistry from our network in disks to earlier works on hot cores, disks, AGB stars, and planetary atmospheres as described below.

5.1. Acetylene

Comparing to previous disk studies, we find that the mechanism to unlock C from CO is the same as described in Bast et al. (2013, as well as the references therein) and Walsh et al. (2015): CO is either photodissociated to C or reacts with He^+ produced by CR or X-ray photons (depending on which one dominates) to form C^+. The chemistry pathways to form C_2H_2 shown in these studies are similar to what we found in our work. Walsh et al. (2015) did not find the neutral-neutral formation pathway to C_2H from C_2 important. Our chemistry is also similar to that in Agúndez et al. (2008), although their models begin to form CH by C abstracting H from H_2. This reaction has a high energy barrier (12 000 K) and is also reported in Walsh et al. (2015). Despite having this reaction in our disk models, we formed CH via radiative association of C and H and destruction of CH_2 which is a barrier-free reaction and has no temperature dependence. This difference arises because Agúndez et al. (2008) follow the time-dependent evolution of chemistry with hydrogen being initially molecular.

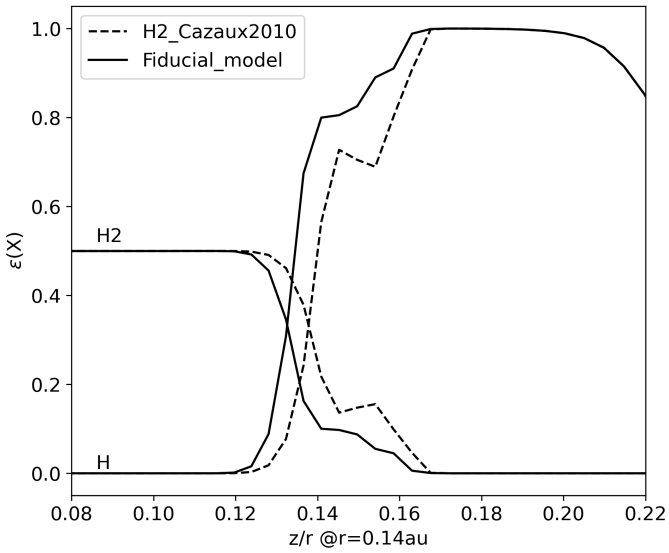

Fig. 13. Effect of using updated H_2 formation rate of Cazaux & Tielens (2010) compared to Cazaux & Tielens (2004) on the H→ H_2 transition layer. The figure compares the fiducial model using the large DIANA chemistry with the disk having the extended chemical network using the formation mechanism and the energy barrier reported in Cazaux & Tielens (2010).

Warm carbon chain chemistry (WCCC) sources are Class 0/I objects that contain hydrocarbons (e.g. L1527; Sakai et al. 2008). The densities in WCCCs are of the order of $10^9 cm^{-3}$ and temperatures are ~300 K. The chemistry is initiated by sublimating methane ice, which subsequently reacts with C^+ to form hydrocarbon molecules (Sakai & Yamamoto 2013). The formation of higher hydrocarbons proceeds via addition of C^+ followed by dissociative recombination with e^- or via reaction with CH_4 (Sakai & Yamamoto 2013). The chemistry is completely dominated by ion-neutral chemistry. In our disk models (i.e. point 1 which has similar density, temperatures as WCCC sources; see Fig. 1), we find that reactions with C tend to dominate over reactions with C^+. Higher hydrocarbons are formed also via addition of neutral C. Addition of H_2 to ions is the main pathway in disks to form higher hydrogenated ion contrary to the addition of CH_4 to molecular ions which occurs in WCCC sources. The high abundances of C^+ required in WCCC sources are maintained either by high cosmic-ray induced ionization (ζ) or high UV. WCCCs can have $\zeta \geq 10^{-16} s^{-1}$ (Kalvāns 2021), whereas we use $\zeta = 10^{-17} s^{-1}$ in our disk models. We used a steady-state chemistry model while the WCCC models study

time-dependent chemistry starting from cold icy conditions in dark cores and warming up over short timescales as gravitational collapse provides energy. So there is also a fundamental difference in timescales of chemistry and history of material.

C-rich Asymptotic giant branch (AGB) stars have been studied in detail by, for example Cherchneff & Glassgold (1993); Millar & Herbst (1994). Typical gas temperatures in the inner circumstellar envelopes around AGB stars are ∼1000 K and densities are on the order of 10^{10} cm^{-3}. The neutral-neutral chemistry dominates in these objects while the chemistry in disk surface layers that have similar physical conditions (see Fig. 1) is a mixture of ion-neutral and neutral-neutral chemistry. The difference in the initial abundances between our disk model and that of Cherchneff et al. (1993, Table 2) prevents a direct comparison. The trend of an odd-even effect where even numbered C hydrocarbons are more abundant than the odd C (see Cherchneff & Glassgold 1993, Fig. 3) is also seen in our disk models.

Loison et al. (2019) and Vuitton et al. (2019) studied the hydrocarbon chemistry in atmospheres of planets and moons. The chemical networks in these studies take into account the termolecular and pressure dependent reactions. The temperatures range from ∼80 to 180 K and pressures vary from 10^5 (surface) to 10^{-7} Pascal with altitude (Hörst 2017). These pressures correspond to a range of ∼10^8 to 10^{20} cm^{-3} of particle densities. The reactions destroying C_2H_2 to form C_2H and C_2 in atmospheres (Vuitton et al. 2019) are also dominant in the disk surface layers but the physical conditions are not the same, thus preventing an in depth comparison.

5.2. Benzene

Reactions (20)–(22) forming C_6H_6 are the dominant pathways in both studies (Loison et al. 2019; Vuitton et al. 2019). We find the same reactions to be the major pathways forming benzene in the disk. The reaction

$$C_3H_3 + C_3H_3 + M \rightarrow C_6H_6 + M \quad (25)$$

is found to contribute to form benzene at pressures ∼10^{15} to 10^{19} cm^{-3} and at temperatures of ∼160 K in atmospheres (Loison et al. 2019). However, Woods & Willacy (2007) included this reaction and did not find it to be important in disks; therefore not included in our network.

On comparing the benzene formation routes in models using the UMIST2012 and KIDA2014 database the formation scheme via reactions (20) and (21) leading to C_6H_6 are reported in McEwan et al. (1999) for the interstellar medium and are dominant in both the models. The reaction scheme forming benzene in protostellar environments outlined in Woods & Willacy (2007) as

$$CH_3CCH + C_3H_4^+ \rightarrow C_6H_7^+ + H \quad (26)$$

is not dominant in any of our models. The thermal decomposition reaction of CH_2CCH with M to form C_2H_2 becomes dominant and is favoured over the neutral-neutral reaction of CH_2CCH with H_2 forming CH_3CCH. This decreases the abundance of CH_3CCH, resulting in reaction (26) not being dominant.

5.3. Future work

A chemical network can never be complete. Based on the species for which the reactions of formation and destruction were available, the extended network for hydrocarbon chemistry is provided. The difference in rate coefficients from the rate databases affects the chemistry and the abundance of species in the disk, but we show that the impact on the observable C_2H_2 line fluxes is lower than a factor of 2.

The values of adsorption energies shift the ice lines and the uncertainties in these thus affect the chemistry. Laboratory measurements of enthalpy of formation for a number of higher hydrocarbon ions are needed as they can also affect the chemical structure of the disk. We also miss species from the chemical network as we are limited by the rate databases. Our network does not include C_6H_5 or C_6H_4 (as explained in Sect. 2.3).

A clear distinction between the isotopomers of species and their rate coefficients needs to be included in the rate databases. KIDA has more species compared to KIDA2014, but it is not in the format of an easy to use ratefile. Often multiple rate coefficients exists and so the user has to decide which rates are better. In addition, the database changes constantly, causing an issue to reproduce results at a later stage. These are fundamental differences to UMIST which clearly recommends rates and has stable releases. Both approaches of course have their pros and cons.

We lack currently the framework to fully take into account the pressure-dependent reactions in PRODIMO which are dominant in planetary atmospheres. Adding these is beyond the scope of this paper and will be the subject of a future study. These reactions might be important in the midplane (point 3) but less so in the surface layers of the disks. It is necessary to test in the future the importance of such reactions for the high density inner disks as we may miss some key pathways.

6. Conclusion

In this paper, we aim to understand the hydrocarbon chemistry in the inner, warm, and dense regions of planet-forming disks around T Tauri stars. We present an extended chemical network that includes hydrocarbon species with up to eight carbon atoms. It includes the linear and cyclic isotopomers of several species, limited by the availability of such data in UMIST2012 and KIDA2014. With this network, we can form the simplest cyclic hydrocarbon: benzene.

We find that a more extended chemistry alone does not explain the high fluxes observed by *Spitzer*. A more detailed study varying physical parameters of the disk using this chemical network is needed to better interpret the observations. We find that the abundances of C_2H_2 using the extended chemical network increase only by ∼40% relative to the large DIANA chemical network in the surface layers (grid point 1). The reservoir of gas-phase C_2H_2 in the outer midplane disappears to form ices of longer hydrocarbons. The abundance in those regions thus drops by seven orders of magnitude (grid point 2). There is a decreasing gradient of C_2H_2 abundance in the inner midplane, which is more prominent in the model using the extended chemical network (model 5). With the expanded network, we find that in extremely inner regions of the disk the major C_2H_2 formation pathways were balanced by the neutral-neutral, three body, or thermal decomposition destruction pathways making secondary species such as H_2O, NH_3 etc important. A detailed analysis of the three-body reactions network is needed and will be the focus of a subsequent paper.

H, H_2, C, and C^+ are crucial to form C_2H_2. Therefore, the layer at which the H/H_2 transition occurs is important and thus the details of the H_2 formation mechanism. We find that this transition occurs higher up in the disk when using the updated formalism of H_2 formation (Cazaux & Tielens 2010). This is also

important in determining the radial extent of the surface layer where C_2H_2 is abundant.

The extended chemical network presented here, is important when studying longer hydrocarbons in the disks. With JWST discovering more complex hydrocarbon species in disks, an extensive chemical modelling is warranted. Our work thus presents a key step forward in modelling the hydrocarbons in disks for future comparisons with JWST observations.

Acknowledgements. This project has received funding from the European Union's Horizon 2020 research and innovation programme under the Marie Sklodowska-Curie grant agreement No. 860470. C.H.R. acknowledges the support of the Deutsche Forschungsgemeinschaft (DFG, German Research Foundation) research Unit "Transition discs" – 325594231. C.H.R. is grateful for support from Max Planck Society. We thank the anonymous referee for their constructive comments.

References

Agúndez, M., Cernicharo, J., & Goicoechea, J. R. 2008, A&A, 483, 831
Anderson, D. E., Blake, G. A., Cleeves, L. I., et al. 2021, ApJ, 909, 55
Arabhavi, A. M., & Kamp, I. 2023, Science, submitted
Bast, J. E., Lahuis, F., van Dishoeck, E. F., & Tielens, A. G. G. M. 2013, A&A, 551, A118
Bergin, E. A., Du, F., Cleeves, L. I., et al. 2016, ApJ, 831, 101
Bethell, T., & Bergin, E. 2009, Science, 326, 1675
Carr, J. S., & Najita, J. R. 2011, ApJ, 733, 102
Cazaux, S., & Tielens, A. G. G. M. 2004, ApJ, 604, 222
Cazaux, S., & Tielens, A. G. G. M. 2010, ApJ, 715, 698
Cherchneff, I., & Glassgold, A. E. 1993, ApJ, 419, L41
Cherchneff, I., Glassgold, A. E., & Mamon, G. A. 1993, ApJ, 410, 188
Draine, B. T., & Bertoldi, F. 1996, ApJ, 468, 269
Duval, S. E., Bosman, A. D., & Bergin, E. A. 2022, ApJ, 934, L25
Greenwood, A. J., Kamp, I., Waters, L. B. F. M., Woitke, P., & Thi, W. F. 2019a, A&A, 626, A6
Greenwood, A. J., Kamp, I., Waters, L. B. F. M., Woitke, P., & Thi, W. F. 2019b, A&A, 631, A81
Guzmán, V. V., Bergner, J. B., Law, C. J., et al. 2021, ApJS, 257, 6
Heays, A. N., Bosman, A. D., & van Dishoeck, E. F. 2017, A&A, 602, A105
Henning, T., & Semenov, D. 2013, Chem. Rev., 113, 9016
Hörst, S. M. 2017, J. Geophys. Res. Planets, 122, 432
Ilee, J. D., Walsh, C., Booth, A. S., et al. 2021, ApJS, 257, 9
Kalvāns, J. 2021, ApJ, 910, 54
Kamp, I., Tilling, I., Woitke, P., Thi, W. F., & Hogerheijde, M. 2010, A&A, 510, A18
Kamp, I., Thi, W. F., Woitke, P., et al. 2017, A&A, 607, A41
Kress, M. E., Tielens, A. G. G. M., & Frenklach, M. 2010, Adv. Space Res., 46, 44
Loison, J. C., Dobrijevic, M., & Hickson, K. M. 2019, Icarus, 329, 55
McElroy, D., Walsh, C., Markwick, A. J., et al. 2013, A&A, 550, A36
McEwan, M. J., Scott, G. B. I., Adams, N. G., et al. 1999, ApJ, 513, 287
Meijerink, R., Aresu, G., Kamp, I., et al. 2012, A&A, 547, A68
Millar, T. J., & Herbst, E. 1994, A&A, 288, 561
Pontoppidan, K. M., Salyk, C., Blake, G. A., et al. 2010, ApJ, 720, 887
Qi, C., Öberg, K. I., Wilner, D. J., & Rosenfeld, K. A. 2013, ApJ, 765, L14
Rab, C., Güdel, M., Woitke, P., et al. 2018, A&A, 609, A91
Rimmer, P. B., & Helling, C. 2016, ApJS, 224, 9
Rothman, L. S., Gordon, I. E., Barbe, A., et al. 2009, J. Quant. Spec. Radiat. Transf., 110, 533
Sakai, N., & Yamamoto, S. 2013, Chem. Rev., 113, 8981
Sakai, N., Sakai, T., Hirota, T., & Yamamoto, S. 2008, ApJ, 672, 371
Salyk, C., Pontoppidan, K. M., Blake, G. A., et al. 2008, ApJ, 676, L49
Santoro, G., Martínez, L., Lauwaet, K., et al. 2020, ApJ, 895, 97
Tabone, B., Bettoni, G., van Dishoeck, E. F., et al. 2023, Nat. Astron., 7, 805
Vuitton, V., Yelle, R. V., Klippenstein, S. J., Hörst, S. M., & Lavvas, P. 2019, Icarus, 324, 120
Wakelam, V., Herbst, E., Loison, J. C., et al. 2012, ApJS, 199, 21
Wakelam, V., Loison, J. C., Herbst, E., et al. 2015, ApJS, 217, 20
Walsh, C., Nomura, H., & van Dishoeck, E. 2015, A&A, 582, A88
Woitke, P., Kamp, I., & Thi, W. F. 2009, A&A, 501, 383
Woitke, P., Min, M., Pinte, C., et al. 2016, A&A, 586, A103
Woitke, P., Min, M., Thi, W. F., et al. 2018, A&A, 618, A57
Woitke, P., Thi, W.-F., Arabhavi, A. M., et al. 2023, A&A, in press, https://doi.org/10.1051/0004-6361/202347730
Woods, P. M., & Willacy, K. 2007, ApJ, 655, L49

Appendix A: Reactions taken from STAND2020

Table A.1. List of three-body and thermal-decomposition reactions added.

Reactions	α	β	γ
CH + M → C + H + M	3.16E-10	0.00E+00	3.37E+04
CN + M → C + N + M	1.09E-9	0.00E+00	7.10E+04
H + H + M → H_2 + M	9.13E-33	-6.00E-01	0.00E+00
H + N + M → NH + M	5.02E-32	0.00E+00	0.00E+00
N + N + M → N_2 + M	1.25E-32	0.00E+00	0.00E+00
N + O + M → NO + M	3.26E-33	0.00E+00	0.00E+00
C_2H + M → C_2 + H + M	5.00E-01	-5.16E+00	5.74E+04
C_2O + M → C_2 + O + M	5.00E-01	-5.16E+00	5.74E+04
CH_2 + M → CH + H + M	9.33E+00	0.00E+00	4.51E+04
HCN + M → HNC + M	1.45E-06	1.00E+00	2.38E+04
CN + H + M → HCN + M	9.35E-30	-2.00E+00	5.20E+20
CO + O + M → CO_2 + M	1.20E-32	0.00E+00	2.16E+03
NH_2 + M → NH + H + M	1.99E-09	0.00E+00	3.83E+04
H + CH_2 + M → CH_3+ M	5.63E-31	0.00E+00	0.00E+00
NH_3 + M → NH + H_2 + M	1.05E-09	0.00E+00	4.70E+04
OCN + M → CO + N + M	3.95E-06	-1.90E+00	3.01E+04
H + C_2H + M → C_2H_2 + M	2.63E-26	-3.10E+00	7.21E+02
H_2CO + M → CO + H_2 + M	9.40E-09	0.00E+00	3.32E+04
C_2H_2 + M + H → M + C_2H_3 + M	4.87E-30	-1.07E+00	8.38E+01
H + C_2H_4 + M → C_2H_5 + M	9.23E-29	-1.51E+00	7.29E+01
H + C_2H_5 + M → CH_3CH_3 + M	2.00E-28	-1.50E+00	0.00E+00
H + C_2H_3 + M → C_2H_4 + M	1.49E-29	-1.00E+00	0.00E+00
CH_2OH + M + H → CH_3OH + M	1.20E-29	1.04E+00	0.00E+00
CH_3O + H + M → CH_3OH + M	7.21E-30	1.24E+00	0.00E+00
H_2CO + H + M → CH_3O + M	1.80E-31	6.60E-01	8.63E+02
CH_2OH + M → H_2CO + H + M	1.66E-10	0.00E+00	1.26E+04
C_2H + M → C_2 + H + M	5.00E-01	-5.16E+00	5.74E+04
C_2O + M → C_2 + O + M	5.00E-01	-5.16E+00	5.74E+04
H + C_2H_3 + M → C_2H_4 + M	1.49E-29	-1.00E+00	0.00E+00
C_2H_4 + M → C_2H_2 + H_2 + M	5.80E-08	0.00E+00	3.60E+00
H + C_4H + M → HC_4H + M	2.64E-26	-3.10E+00	7.21E+02
C_2H + C_2H + M → HC_4H + M	5.56E-28	-3.00E+00	3.00E+02
H + C_4H_3 + M → CH_2CHCCH + M	5.41E-23	-3.97E+00	1.77E+02
H + HC_4H + M → C_4H_3 + M	3.53E-25	-2.93E+00	1.76E+02
C_2H_2 + C_2H_2 + M → CH_2CHCCH + M	3.78E-31	1.00E+00	1.86E+00
CH_3CH_3 + M → C_2H_4 + H_2 + M	3.80E-07	0.00E+00	3.40E+04
CH_2CCH + M → C_2H_2 + CH + M	1.00E-14	0.00E+00	0.00E+00
C_4H_3 + M → C_2H_2 + C_2H + M	5.34E-05	1.00E+00	4.15E+04
H + e^- + M → H^- + M	2.50E-31	-1.50E+00	0.00E+00
HS + H + M → H_2S + M	1.00E-30	-2.00E+00	0.00E+00
H_2 + S + M → H_2S + M	1.40E-31	-1.90E+00	8.14E+03
CO + S + M → OCS + M	3.00E-33	0.00E+00	1.00E+03
CH_3^+ + H_2 + M → CH_5^+ + M	1.10E-28	0.00E+00	0.00E+00
$C_2H_2^+$ + C_2H_2 + M → $C_4H_4^+$ + M	1.60E-26	0.00E+00	0.00E+00
$C_2H_2^+$ + H_2 + M → $C_2H_4^+$ + M	1.20E-27	0.00E+00	0.00E+00
$C_2H_3^+$ + H_2 + M → $C_2H_5^+$ + M	1.49E-29	0.00E+00	0.00E+00

We list the three-body and thermal-decomposition reactions that are taken from STAND2020 network and included in our models. As three-body reactions are pressure-dependent, we take the low-pressure rate coefficients for these reactions. A detailed analysis to formulate a complete three-body reaction network will be left for a future work.

Appendix B: C_2H_2 formation/destruction pathways in KIDA2014

The following figures show the major formation and destruction pathways leading to C_2H_2 when using the KIDA2014 database in model 2 (using large DIANA network) and model 4 (using extended hydrocarbon network).

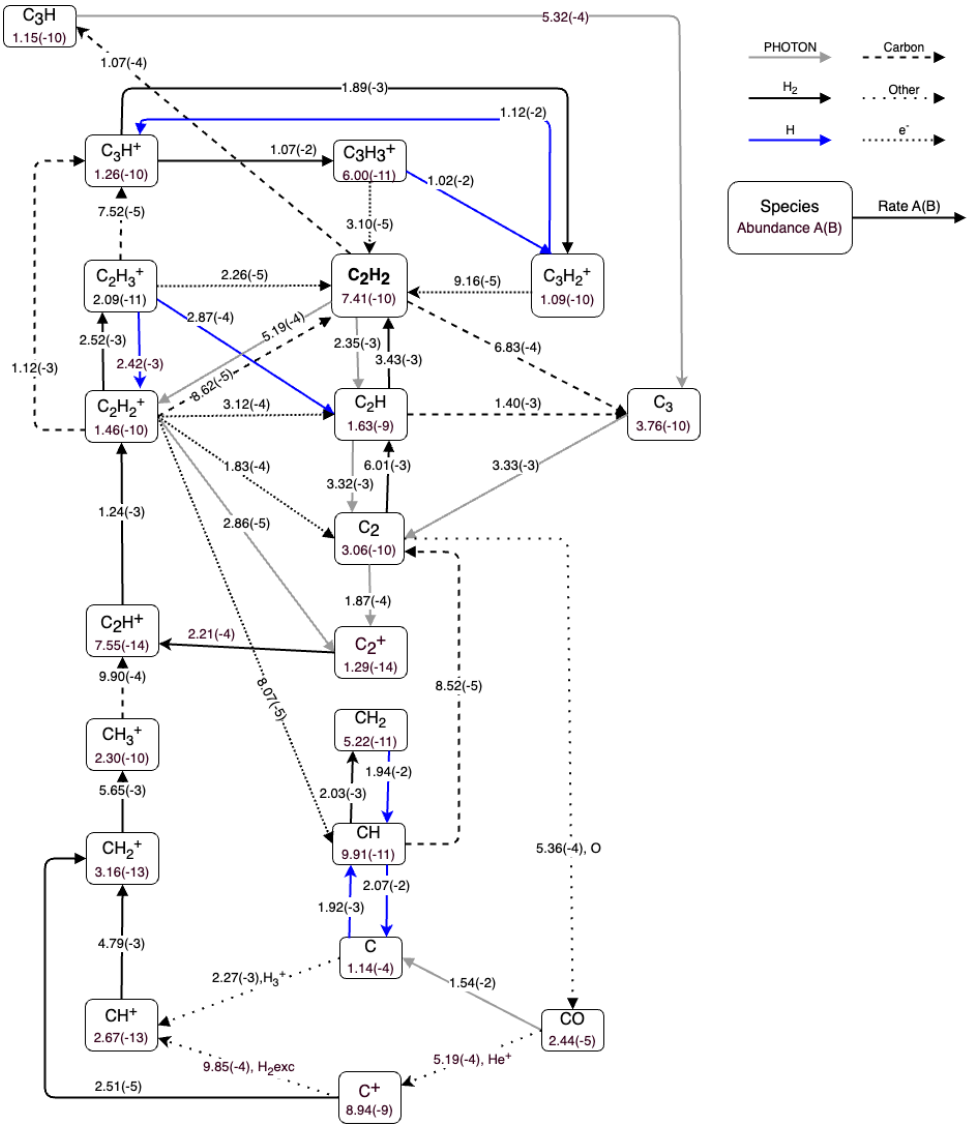

Fig. B.1. Chemical network centered around C_2H_2 depicting the dominant formation and destruction pathways of parent molecules for model 2 (large DIANA network using the KIDA2014 rate database).

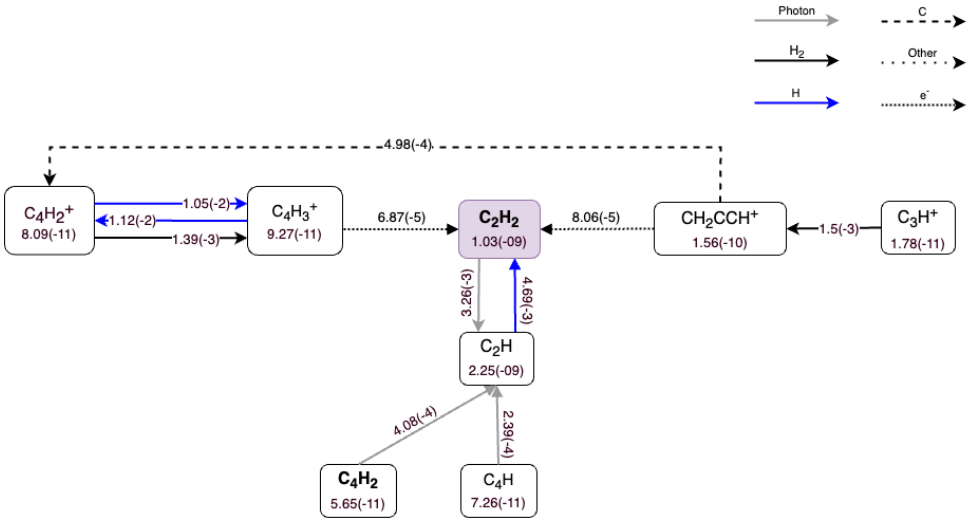

Fig. B.2. Zoomed-in chemical network for the extended hydrocarbon chemistry in model 4 (KIDA2014) showing the new pathways forming C_2H_2 and C_2H that were not dominant in model 2 (UMIST2012). Only two steps in the formation pathway are shown.